Bull. Mater. Sci., Vol. 35, No. 3, June 2012, pp. 471–480. © Indian Academy of Sciences.

A comprehensive study on influence of Nd^{3+} substitution on properties of $LiMn_2O_4$

S BALAJI*, T MANICHANDRAN and D MUTHARASU†
Department of Chemistry, Thiagarajar College of Engineering, Madurai 625 015, India
†School of Physics, Universiti Sains Malaysia, Penang 11030, Malaysia

MS received 31 March 2011; revised 27 July 2011

Abstract. **$LiNd_xMn_{2-x}O_4$ samples are synthesized via co-precipitation technique. The activation energies computed from thermogravimetric analyses on the basis of Ozawa method have been observed to linearly increase with increase in dopant concentration. X-ray diffraction analyses indicate the cubic–spinel structure for all the samples. The lattice parameter has been observed to decrease with increasing concentration of Nd^{3+} doping. The octahedral site preference of neodymium dopant in the $LiMn_2O_4$ structure has been elucidated using XRD and FT–IR studies. The porosity and surface roughness obtained from SEM analysis have been observed to decrease with increase in Nd^{3+} dopant concentration in $LiMn_2O_4$ lattice. The electrochemical performances of the electrodes were analysed through cyclic voltammetry, chronopotentiometry and electrochemical impedance techniques. The specific capacity has been observed to decrease initially with increase in Nd^{3+} dopant concentration, whereas the capacity retention has increased with increase in dopant concentration. The observed percentage capacity retention after 50 cycles of the electrodes $LiNd_{0.05}Mn_{1.95}O_4$, $LiNd_{0.10}Mn_{1.90}O_4$ and $LiNd_{0.15}Mn_{1.85}O_4$ were 88·4%, 97·1% and 96·8%, respectively. The Li ion diffusion coefficient ascertained using electrochemical impedance spectroscopy was found to be higher for $LiNd_{0.10}Mn_{1.90}O_4$ around $3{\cdot}74 \times 10^{-12}$ $cm^2\,s^{-1}$.**

Keywords. **Co-precipitation; rare earth doping; Ozawa method; lithiation; cycle life.**

1. Introduction

Lithium manganese oxide is one among the prominent electrode materials for secondary lithium ion battery. Lithium manganese oxide with cubic spinel structure has attracted great deal of attention due to its advantages like low cost, abundance of manganese in earth crust, environmental harmlessness and high theoretical lithiation capacity (∼148 mAh/g) (Aurbach *et al* 1999). Inspite of its unique advantages, it possesses certain drawbacks like capacity fading on prolonged cycling, manganese dissolution into the electrolyte and structural instability on cycling (Xia *et al* 1997). The above mentioned defects are attributed to the structural distortion mechanism called Jahn Teller distortion, which arises in the presence of unpaired electrons and unbalanced electron distribution in t_2^g and e_g electronic d orbitals. In $LiMn_2O_4$, Mn^{3+} ion is prone to Jahn Teller distortion due to the presence of single unpaired electron in e_g orbital (Chung and Kim 2004). Hence the effective way to check the capacity fading would be the reduction of Mn^{3+} concentration, but it may result in lower specific capacity because, the concentration of Mn^{3+} and Mn^{4+} plays a major role in determining the specific capacity (Fey *et al* 2003). Therefore, there should be a trade-off between the specific capacity and capacity retention of $LiMn_2O_4$. With this idea, in this paper we propose the substitution of trace amount of neodymium instead of Mn^{3+} ion into the crystal lattice of $LiMn_2O_4$ to improve the capacity retention and to maintain capacity above certain level.

The synthesis of Nd^{3+} substituted $LiMn_2O_4$ has been carried out using hybrid co-precipitation method due to the comfortableness in maintaining the lithium concentration, which is the main drawback in most of the dry and wet chemical synthetic procedures (Denga *et al* 2004). This paper has been primarily attributed to the influence of Nd^{3+} substitution in structural, morphological, thermal and electrochemical properties of $LiMn_2O_4$.

2. Experimental

The Nd^{3+} substituted lithium manganese compounds with general formula, $LiNd_xMn_{2-x}O_4$ ($x = 0{\cdot}05$, $0{\cdot}1$ and $0{\cdot}15$), were synthesized from the chemicals $Nd(NO_3)_3 \cdot 6H_2O$ (Sigma Aldrich), $Mn(CH_3COO)_2 \cdot 9H_2O$ (Sigma Aldrich), NaOH (Aldrich) and $LiOH \cdot H_2O$ (Aldrich). Initially various concentrations of manganese neodymium hydroxides were prepared using co-precipitation of stoichiometric quantities of neodymium and manganese salts with NaOH. The precipitation was carried out with continuous stirring of the reactants in 40 rpm speed using magnetic stirrer, and pH and temperature were maintained at 10·0 and 60°C, respectively. The obtained precipitates were dried in vacuum to remove

*Author for correspondence (sbalaji@tce.edu)

the adsorbed water and grounded well with $LiOH \cdot H_2O$ powders and subjected to 1 h calcinations at 500°C, followed by sintering at 800°C for 20 h in ambient atmospheric condition.

The compound formation kinetics in the ambient atmosphere was studied by thermogravimetry and differential thermal analysis using SII Exstar 6000 TG/DTA equipment. In order to find the activation energy needed for the reaction, the precursors prior to calcination were subjected to thermal analysis at three different scan rates viz. 5°C/min, 10°C/min and 15°C/min. The thermograms of each sample obtained at three different heating rates were analysed using TG kinet software and the activation energy needed for the synthesis was calculated on the basis of Ozawa (1970) method. The sintered compounds were subjected to structural characterization through XRD using PW 1710 diffractometer with automatic data acquisition. All scans were recorded in 2θ range between 10 and 80 degrees. The indexation was carried out in comparison with the JCPDS data. The lattice parameters were calculated using 'Powder-X' software. The structural evaluation was also carried out using FT–IR and Perkin–Elmer FT–IR spectrophotometer in the range 350–1000 cm^{-1}. The compounds were mixed with excess amount of KBr and pelletized into 1·3 cm diameter pellet prior to FT–IR analysis. All the presented FT–IR spectra were recorded after five initial scans. The chemical compositions of the compounds were determined by Thermo Electron IRIS intrepid II XSP Duo Inductively coupled plasma – atomic emission spectrophotometer. Prior to chemical analysis, the samples were microwave digested in concentrated HCl. The scanning electron microscopy was performed using JEOL, JSM-6460 equipment. Three representative areas were randomly selected and scanned in vertical direction and a series of sequential images were recorded for each selected area. The particle sizes of the samples were analysed using laser photo cross correlation technique provided by Nanophox Sympatec particle size analyser.

A three-electrode glass cell, consisting of a working electrode, reference and counter electrode were used for cyclic voltammetric measurements. The working electrodes were cast on an Al foil using doctor blade method. Electrodes with an area of 1 cm^2 for the measurements of electrochemical characterization were prepared by coating slurries (about 100 μm in thickness) on aluminum foils followed by drying in vacuum at 60 for 12 h. The slurry used for electrode coating was prepared using *N*-methyl pyrolidone along with the mixture of synthesized material, conducting agent (acetylene black) and PVdF (poly vinylidine fluoride) in the ratio (80:15:5%). Lithium foil was used as both reference and counter electrodes. The working electrode and lithium foil were separated by polypropylene separator (Celgard). The $LiPF_6$ (Aldrich) in 1:1 (wt%) of ethylene carbonate (Alfa easer) and dimethyl carbonate (DMC), (Aldrich), was used as the electrolyte throughout the study. The cyclic voltammetry measurements and chronopotentiometry were performed with PGSTAT and μAutolab III with FRA 2 electrochemical system. The cyclic voltammetry analyses were performed at 50 mV/s rate and the chronopotentiometry studies were performed in galvanostatic condition with a current of 100 μA. The electrochemical impedance analyses were carried out in the range 10 mHz–10^5 Hz using frequency response analyser.

3. Results and discussion

3.1 *Thermal analysis*

The compound formation kinetics has been analysed using thermogravimetry analysis (TGA). The results of thermogravimetry analyses of the samples are presented in figure 1(a).

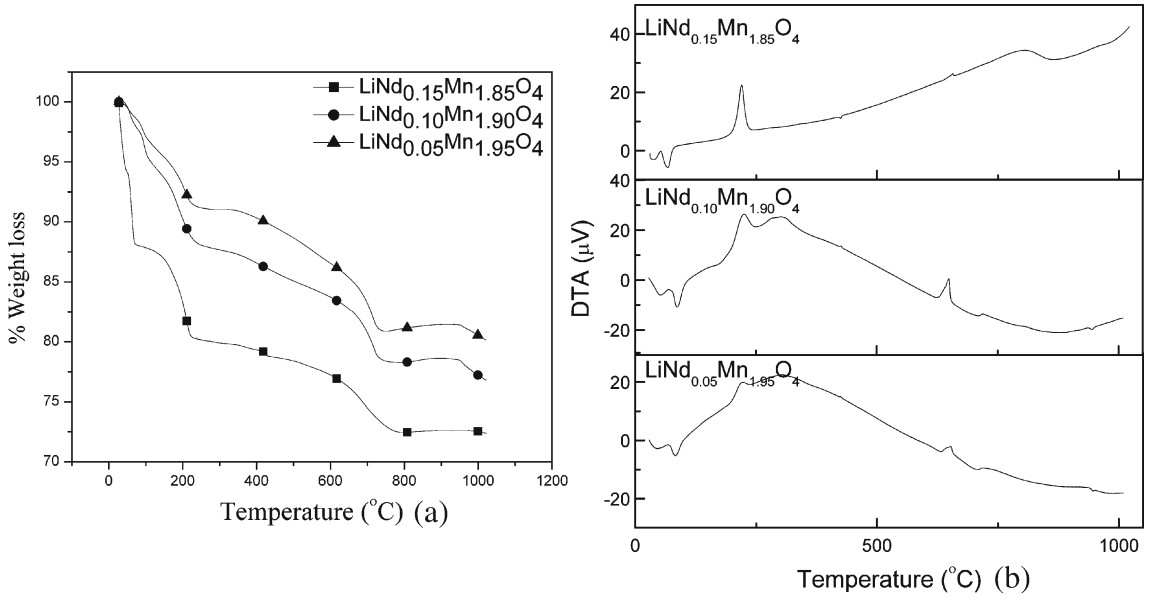

Figure 1. (**a**) TGA and (**b**) DTA analyses results of $LiNd_xMn_{2-x}O_4$ samples.

Table 1. Thermal analysis and chemical composition parameters.

Sample	Weight loss temperatures (°C)				Activation energy (kJ/mol)	Chemical composition (ICP–AES)					
						Wt% (±0·01)			Ratio		
	I	II	III	IV	(±0·2)	Li	Mn	Nd	Li	Mn	Nd
$LiNd_{0.05}Mn_2O_4$	62·5	199·8	425·3	683	185·4	4·65	70·15	3·98	1·02	1·941	0·042
$LiNd_{0.10}Mn_2O_4$	79·6	306·1	418·2	664	197·7	4·63	68·74	9·28	1·013	1·902	0·0978
$LiNd_{0.15}Mn_2O_4$	65·1	307·5	426·5	657·3	237·3	4·67	66·97	13·58	1·023	1·853	0·1432

All the samples have been observed to possess weight loss in four steps. The initial weight loss around 100°C could be attributed to initial dehydration, followed by weight losses around 200°C, 420°C and 675°C corresponding to residual water removal, compound formation and oxidation of unreacted excess LiOH, respectively.

The temperatures of respective weight losses have been observed to increase with increasing dopant concentration. The temperatures corresponding to weight losses observed from TGA are summarized in table 1. The differential thermal analysis (DTA) plot presented in figure 1(b) shows endothermic reaction in elimination of water molecules from the reactants. The oxidation of reactants and compound formation for all the samples has been identified to be exothermic in nature. The activation energy results computed through TG-Kinet software are presented in table 1 which shows increase in activation energy with increasing Nd^{3+} dopant concentration.

3.2 *Compositional analysis*

The results of composition analysis obtained from ICP–AES are presented in table 1. The ratios of lithium concentrations in all the samples have been determined to be more or less the same. The concentration of Mn and Nd has been identified to vary sequentially as expected.

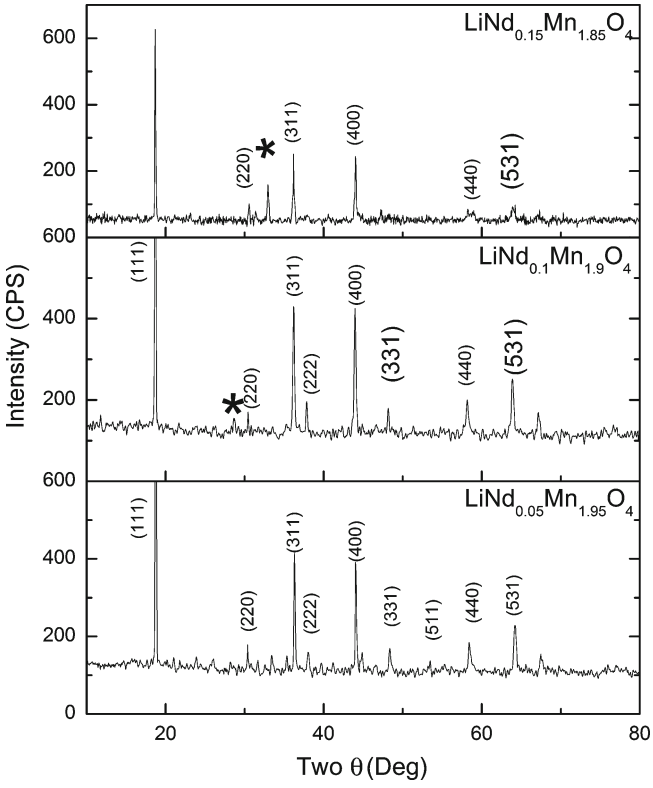

Figure 2. XRD spectra of $LiNd_xMn_{2-x}O_4$ samples ($NdMnO_3$ phase).

3.3 *Structural analysis*

The X-ray diffractogram of the powders $LiNd_xMn_{2-x}O_4$ ($x = 0{\cdot}05$, $0{\cdot}10$ and $0{\cdot}15$) are presented in figure 2. All the diffractograms have been observed to possess predominant orientations corresponding to spinel cubic lattice orientations (111), (311), (400) and (440), respectively. The existence of the above peaks confirm isostructural cubic crystalline nature of all the compounds irrespective of dopant concentration (Arora *et al* 1998). The site occupancy of Li ions in the host matrix is an important factor that determines the electrochemical properties of the system (Thackeray *et al* 1983; Thackerey and Rossouw 1994). Ohzuku *et al* (2001) used the integrated intensity ratios of close-lying peaks in the XRD spectra to determine the extent of occupancy of substituent ions.

According to Ohzuku *et al* (2001), the integrated intensity ratios of the (400)/(311) and (220)/(311) peaks are an indication of the extent of occupancy of the substituent ions in octahedral (B) and tetrahedral (A) sites, respectively. The ratio of intensity of (220)/(311) and (400)/(311) peaks are given in table 2. The ratio of peaks (220)/(311) has almost remained unaltered on doping, which indicates the unchanged tetrahedral site even after doping. On the other hand, the ratio of (400)/(311) peaks has increased linearly with increasing dopant concentration, which shows change in the octahedral site. This change indicates the octahedral site preference of the Nd^{3+} ion and the gradual replacement of Mn^{3+} ion in the octahedral site.

The observation of small trace of impurity in the crystal structure has been identified for higher doping concentration.

Table 2. Structural parameters from XRD.

Sample	I_{220}/I_{311}	I_{400}/I_{311}	Lattice constant (Å)	Crystallite size (nm) (±0·1)	Cell volume ($\times10^{-30}$)	X-ray density (g/cm^3)	Strain (lines^{-2} m^{-4}) ($\times10^{-2}$) (±0·005)	Dislocation density ($\times10^{18}$ lines/m^2)
$LiNd_{0·05}Mn_2O_4$	0·393	0·89	8·243	37·9	560·2	4·39	0·95	0·000694
$LiNd_{0·10}Mn_2O_4$	0·396	0·94	8·237	38·2	558·9	4·51	0·947	0·000684
$LiNd_{0·15}Mn_2O_4$	0·414	0·98	8·215	57·2	554·4	4·65	0·63	0·000305

Upon comparison with the JCPDS data, it could be identified as $NdMnO_3$ impurity (JCPDS No. 25-0565). For the $LiNd_{0·15}Mn_{1·85}O_4$ sample, the existence of new peak around 32·7 degree corresponding to (112) orientation of $NdMnO_3$ has been observed. In general, mild increment in the intensity of the impurity peaks have been observed with increasing dopant concentration and this increment in intensity shows an increase in $NdMnO_3$ concentration.

The lattice parameter has been calculated using the D_{hkl} utility in powder-x software and presented in table 2. The lattice parameter of the $LiNd_{0·05}Mn_{1·95}O_4$ sample has remained almost unchanged when compared with standard $LiMn_2O_4$ (JCPDS No. 35-0782). On further increase in dopant concentration, the decrement in unit cell parameter has been observed. The observation shows similarity with the observation led by Iqbal and Ahmad (2008) and this could be ascribed to the higher binding energy between $Nd^{3+}-O^{2-}$ bond (703±13 kJ mol^{-1}) (Kerr 2000) when compared to the $Mn^{3+}-O^{2-}$ bond (402 kJ mol^{-1}) (Kerr 2000) and since the metal oxygen bonding increases with doping, the contraction in unit cell volume is quite obvious. The shrinkage in unit cell volume with doping could be clearly understood from the cell volume parameter shown in table 2. The manganese in $LiMn_2O_4$ exists in two oxidation states viz. 3+ and 4+ states. During the Nd^{3+} substitution instead of Mn^{3+} ion, the effective content of manganese decreases. As a result, the ratio of Mn^{3+}/ Mn^{4+} decreases in the newly formed spinel lattice. Since the ionic radius of Mn^{4+} (0·53 Å) is less than ionic radius of Mn^{3+} (0·645 Å), the lattice shrinkage is quite obvious. Similar effect has also been observed by Feng *et al* (2003) for Y^{3+} substitution instead of Mn^{3+} in $LiMn_2O_4$.

The diffractogram shown here has been corrected for instrumental broadening and the respective crystallite sizes have been calculated by Debye–Scherrer formula. The crystallite sizes of all the samples have been observed to lie in the range of 30–70 nm. As the dopant concentration increases, the increment in crystallite size has been observed. The crystal lattice strain has been calculated using the formula provided elsewhere (Lalitha *et al* 2004). In general, in any compound the internal strain and dislocation leading to defects arises due to the various processes involved during compound formation. Moreover, as per Chung and Kim (2004), the electrochemical performance of the $LiMn_2O_4$ electrode for cycling at 4 V region depends on the Li content and the Li content is directly proportional to the strain in the crystal lattice (Chung and Kim 2004). Hence the idea of measuring the internal strain and dislocation density would provide better understanding about the compound formation. The crystallite strain and dislocation density of the samples have been observed to decrease with increase in dopant concentration. Since the dislocation density and strain are the manifestation of dislocation network in the compounds, the decrease in strain and dislocation density when compared to undoped compound indicates the structural stability by neodymium doping.

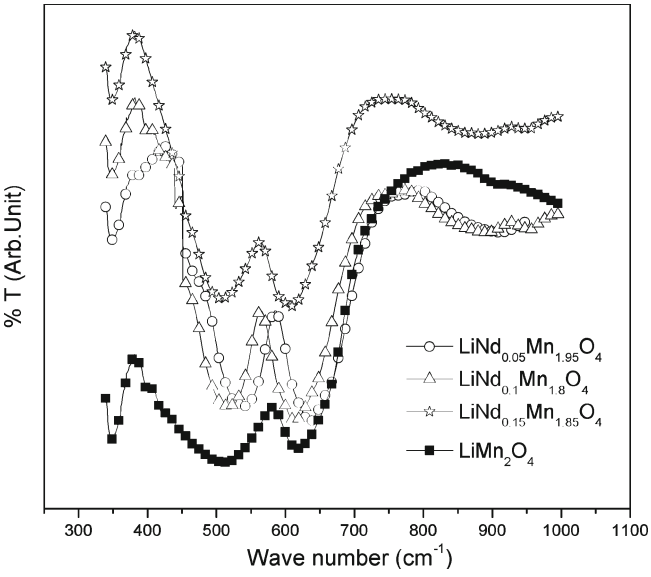

Figure 3. FT–IR vibrational spectra analysis of $LiNd_xMn_{2-x}O_4$.

3.4 *FT–IR analysis*

The infrared transmittance spectrum of the $LiNd_xMn_{2-x}O_4$ ($x = 0, 0·05, 0·1$ and $0·15$) samples are presented in figure 3. For the sake of comparison, FT–IR spectra for $LiMn_2O_4$ has also been added. All the compounds exhibited three predominant vibrational modes respectively to cubic spinel crystal structure around 340 cm^{-1}, 500 cm^{-1} and 620 cm^{-1}. The positions of vibrations corresponding to tetrahedral and octahedral interstices are presented in table 3. The lithium manganese oxide, $LiMn_2O_4$, crystallizes with a cubic spinel-like structure in $Fd3m$ symmetry and has a general structural formula, $A[B_2]O_4$, where B cations reside on the octahedral 16d

Table 3. Force constants from FT–IR spectroscopy.

Sample	ν_1 (Li–O) (cm^{-1})	ν_2^1 (Mn^{IV}–O) (cm^{-1})	ν_2 (Mn^{III}–O) (cm^{-1})	k_t ($\times 10^2$ m^{-1})	k_o ($\times 10^2$ m^{-1})
$LiMn_2O_4$	348	510	619·5	0·669	2·224
$LiNd_{0.05}Mn_2O_4$	346·6	519	635·8	0·6353	2·4507
$LiNd_{0.10}Mn_2O_4$	349	526	633·4	0·6442	2·5238
$LiNd_{0.15}Mn_2O_4$	348·72	507	628·7	0·6431	2·5767

sites, the oxygen anions on the 32*e* sites, and the *A* cations occupy the tetrahedral 8*a* sites. Based on group theoretical calculations of *Fd*3*m* structure, the vibration band around 620 cm^{-1} could be attributed to Mn^{III}–O stretching vibration of MnO_6 groups. Another band of approximately around 500 cm^{-1} could be attributed to the stretching of Mn^{IV}–O bond in octahedral site and this arises due to the charge disproportionation due to two Mn atoms with different charges in $LiMn^{3+}Mn^{4+}O_4$ and the lower wave number peak around 350 cm^{-1} corresponds to the stretching vibration of Li–O bond in tetrahedral site (Julien and Massot 2003; Molenda *et al* 2005). The gradual shift in the band around 620 cm^{-1} has been observed with increase in dopant concentration. This has clearly shown the octahedral site preference of the dopant Nd^{3+} ion and the unaltered tetrahedral band positions further clarify the above inference. As it is known that the decrease in site radius increases the fundamental frequency, the shift towards higher wavenumber clearly emancipates the fact that the doping of Nd^{3+} has led to the decrease in octahedral site radius. This may be due to the higher binding energy between Nd^{3+}–O^{2-} bond when compared to the Mn^{3+}–O^{2-} (402 kJ mol^{-1}) bond and this is in coincidence with the unit volume contraction with doping as observed from XRD.

The site preference of the cations could be well understood from the variation in the force constants of the bond between the cations in the octahedral/tetrahedral sites and oxygen atoms. The force constants, for tetrahedral site (k_t) and octahedral site (k_o), are calculated employing the method suggested by Waldron for cubic spinel compounds (Waldron 1955; Ravinder and Manga 1999; Modi 2004). According to Waldron, the force constants, k_t and k_o, for respective sites are given by

$$k_t = 7{\cdot}62 \times M_1 \times \nu_1^2 \times 10^{-7}, \quad (1)$$

$$k_o = 10{\cdot}62 \times \frac{M_2}{2} \times \nu_2^2 \times 10^{-7}, \quad (2)$$

where M_1 and M_2 are the molecular weights of cations on *A* and *B* sites, respectively.

ν_1 and ν_2 are the vibration bands corresponding to tetrahedral and octahedral bonds. The band positions and force constants are shown in table 3. The octahedral force constants have shown remarkable variation with increasing dopant concentration, whereas the tetrahedral force constants have remained unchanged. Hence the cation distribution in octahedral and tetrahedral sites may be written as (Li^+) $[Nd_x^{3+}Mn_{1-x}^{3+}Mn^{4+}]$ O_4, where atoms shown inside () refers to tetrahedral site and [] refers to octahedral site.

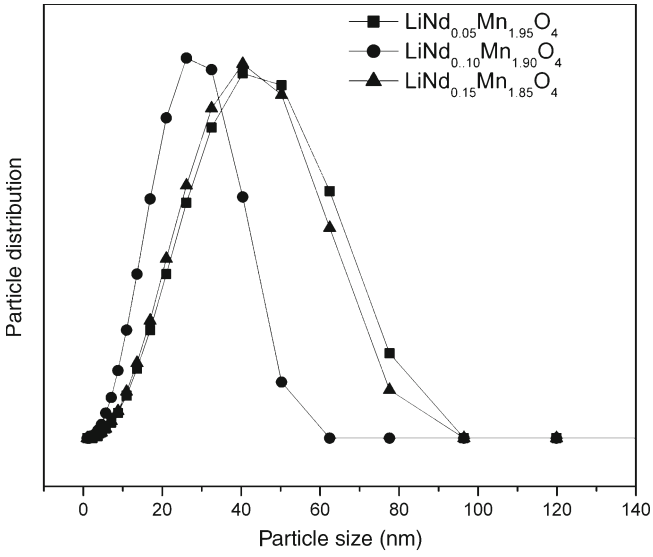

Figure 4. Particle size analysis results of $LiNd_xMn_{2-x}O_4$.

3.5 *Particle size analysis*

The particle size analysis carried out using laser diffraction particle size analyser has been presented in figure 4. The particle size of all the compounds have been observed to be within 100 nm, hence the adopted synthesis condition has been observed to be well suited to prepare nanomaterials with good control over the stochiometry.

3.6 *Morphological analysis*

Scanning electron micrographs depicting morphological features of the $LiNd_xMn_{2-x}O_4$ (x = 0·05, 0·1 and 0·15) are shown in figure 5. The micrographs have been subjected to

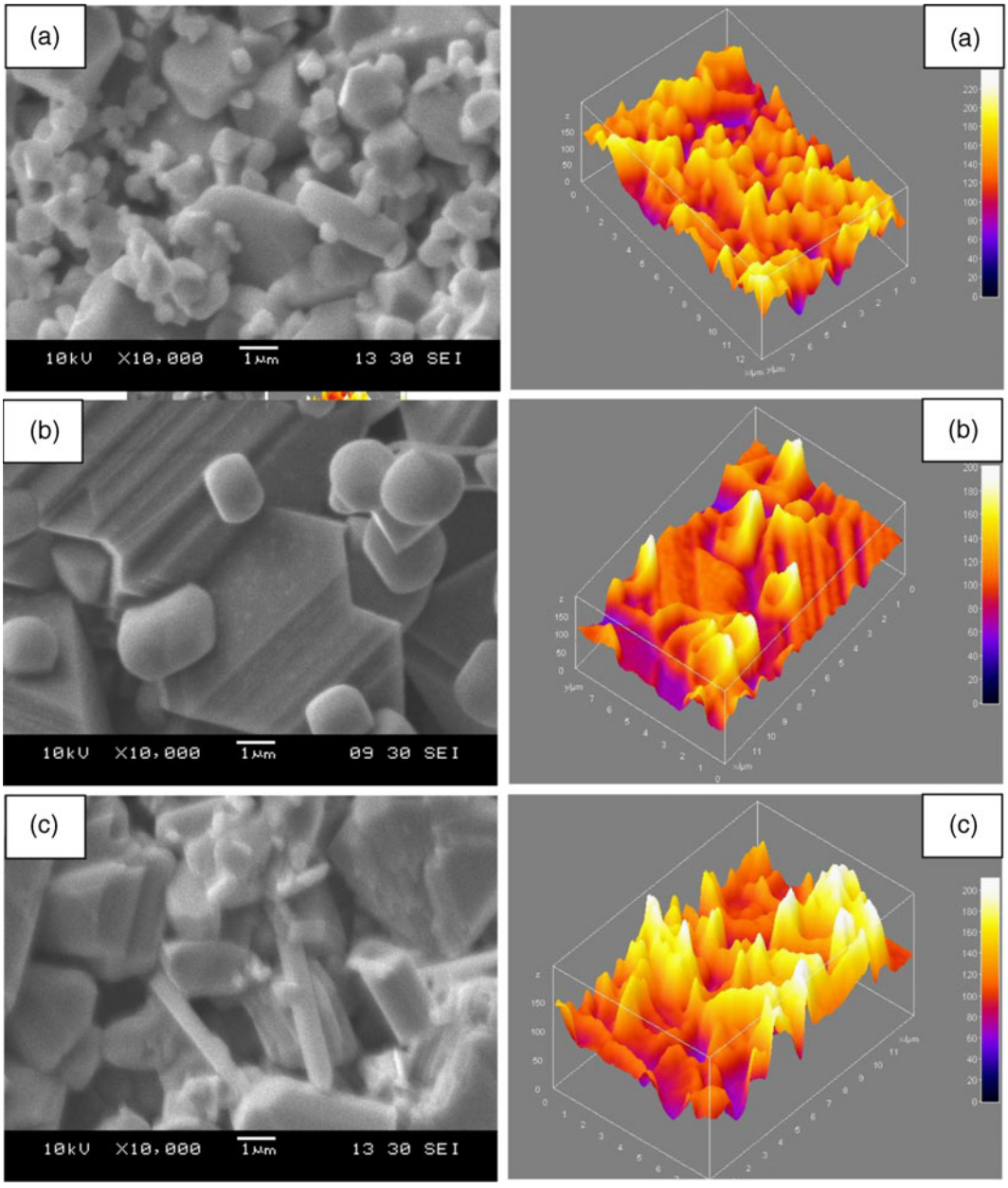

Figure 5. Scanning electron micrograph and 3D surface topography of (**A**) $LiNd_{0.05}Mn_{1.95}O_4$, (**B**) $LiNd_{0.1}Mn_{1.9}O_4$ and (**C**) $LiNd_{0.15}Mn_{1.85}O_4$ samples.

image processing using 'Image-J' software (Image 2002). The image processing has been carried out in four stages viz. de-noising, pore shape regularization, binarization and quantification of relevant features to ascertain porosity, pore size distribution and surface texture. De-noising has been carried out using median filter and the pore shape regularization and binarization have been carried out using 'BinarizeSEM' Java plug-in provided in the software (Balaji *et al* 2010). The porosity, pore area, pore aspect ratio and grain size have been determined by using 'ComputeStats' Java plug-in provided in the software. The observed morphological parameters are presented in table 4. The mean grain size of all the samples has been observed to be between 2 and 6 μm. Though the mean grain size increases with increase in Nd^{3+} concentration, the Nd 0·1 sample shows anomalous behaviour. The agglomerations of grains have been observed in Nd 0·1 sample, but the reason for this anomaly is not clearly known. The average percentage porosity has been observed to decrease with increasing dopant concentration. But the pore aspect ratio has been observed to increase while doping. The pore aspect ratio has direct implications with the electrolyte diffusion into the electrode and thus higher the pore aspect ratios,

Table 4. Morphological parameters.

Sample	Mean grain size (μm) (±0·05)	Porosity (%)	Mean aspect ratio (±0·05)	Roughness	
				R_q (RMS) (nm)	R_a (arithmetic mean) (nm)
$LiNd_{0·05}Mn_2O_4$	2·44	26·2	1·62	134·9	131·0
$LiNd_{0·10}Mn_2O_4$	6·18	15·1	1·65	121·7	117·7
$LiNd_{0·15}Mn_2O_4$	2·78	23·4	1·83	127·7	122·8

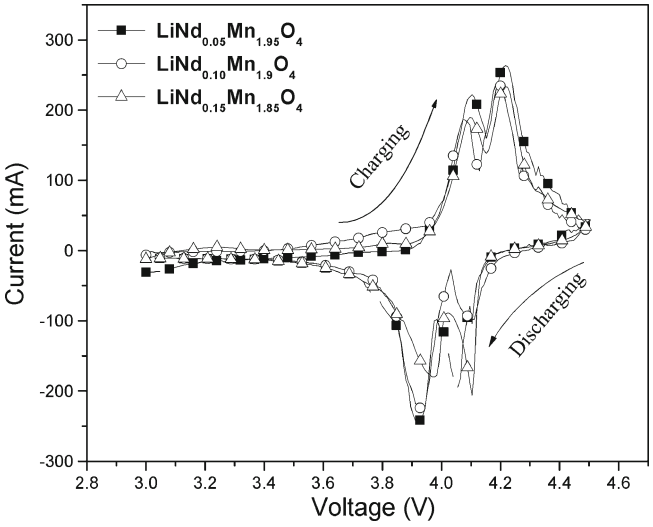

Figure 6. Cyclic voltammetry of $LiNd_xMn_{2-x}O_4$ sample.

higher will be the electrochemical activity of the electrode. Similarly surface roughness shows a decreasing trend with increasing dopant concentration, thus the feasibility to obtain smooth surface with Nd^{3+} doping could be elucidated.

3.7 *Electrochemical analysis*

The first cycle cyclic voltammogram of $LiNd_xMn_{2-x}O_4$ ($x = 0·05$, 0·10 and 0·15) powders are shown in figure 6. The anodic and cathodic peaks observed in figure 6 illustrate reversible oxidation and reduction reactions corresponding to Li extraction and insertion. In the spinel $LiMn_2O_4$, Li ions occupy tetrahedral (8*a*) sites and Mn ions (Mn^{+3}/ Mn^{+4}) occupy octahedral (16*d*) sites. The oxygen ions form a cubic close-packed array, in which tetrahedral (8*a*) sites share face with vacant octahedral sites (16*c*) and thus form three-dimensional vacant channels for Li^+ transport. These channels aid the Li ions to intercalate and de-intercalate through them during the electrochemical reaction. Two separated peaks are expected for both oxidation and reduction, which indicates insertion and extraction of Li ion, occurring in two stages (Santander *et al* 2004).

In general, the 8*a* sites in the spinel form a diamond lattice which can be considered as two interpenetrating *fcc* sublattices separated by (¼ ¼ ¼). For each Li atom, there are four nearest 8*a* neighbours in the other sublattice and six next nearest 8*a* neighbours within the same sublattice. For all the compounds, a clear splitting in oxidation and reduction curves evince the isostructural nature of them. The anodic and cathodic peak potentials of the samples have been presented in table 5. For $LiNd_{0·05}Mn_2O_4$ during charging, the first peak observed at ∼4·096 V is attributed to the removal of Li ions from half of the tetrahedral sites, whereas the second peak found at ∼4·22 V may be due to the removal of Li ions from the remaining (neighbouring) tetrahedral sites (Xia and Yoshio 1996). From figure 6 and table 5, it could be observed that the shifting in peak potentials has taken place with doping. The shifting to lower potential during charging and higher potential while discharging has been observed for higher concentration of Nd^{3+} doping. The splitting of anodic peaks is more pronounced in 0·05 Nd^{3+} atomic concentration samples than the other samples, which elucidates the higher diffusion rate of Li^+ ions in 0·05 doped samples (Ma *et al* 2004).

During doping of Nd^{3+} into the crystal lattice of $LiMn_2O_4$, a general trend of decrease in area covered between oxidation and reduction peaks has been noticed. Since the area is considered as electrochemical active surface area, the observed reduction could be attributed to the reduction in electrochemical activity on doping (Thamizhmani *et al* 2004). Such initial reduction in the electrochemical behaviour could be attributed to the decrease in the concentration of Mn^{3+} ions, which contributes to the charge capacity during inserting and de-inserting of Li^+ ions.

In terms of peak splitting, electrochemical active surface area and intensity of the peaks, the $LiNd_{0·05}Mn_{1·95}O_4$ sample possesses better electrochemical performance than the 0·1 and 0·15 doped sample. Hence, limited addition of rare earth dopant would be preferable to obtain better efficiency.

3.7a *Discharge characteristics*: The galvanostatic discharge curves for the three electrode cells are presented in figure 7. The two distinctive plateaus, characteristic of the well-defined spinel $LiMn_2O_4$ cathode, have been observed for all the samples. The discharge capacities of the samples are presented in table 5. The decrease in the discharge capacity for the initial cycle with neodymium doping has been observed, which is in concurrence with the voltammetry data and is due to the reduction in Mn^{3+} ions as explained above. The observed specific capacities of neodymium doped compounds are higher than the reported value of 120 mAh/g by Yang *et al* (2003).

3.7b *Cycle life studies*: The cyclability of the electrodes tested under identical conditions up to 50 cycles have been presented in figure 8. The percentage capacity retention of samples has been provided in table 5. From figure 8 and table 5, it could be observed that for increasing Nd^{3+} concentration, the capacity retention increases. Especially for the $LiNd_{0.1}Mn_{1.9}O_4$ compound the capacity retention is around 97% which is higher than the rest of the compounds. The capacity retention after 50 cycles for $LiNd_{0.1}Mn_{1.9}O_4$ sample is higher than the values reported by Singhal *et al* (2007) which is around 91% after 25 cycles. Since the capacity fading in $LiMn_2O_4$ is mainly caused by the structural distortion due to Mn^{3+} ion, attempt to decrease the Mn^{3+} ion concentration with Nd^{3+} doping has reduced the structural distortion and has kept the crystal structure intact (Balasubramanian *et al* 2002). Hence the observed improvement in the cyclability is due to the improvement in structural stability by Nd^{3+} doping in $LiMn_2O_4$.

3.7c *Impedance studies*: The Nyquist plots obtained for the samples at 4·2 V after two charge–discharge cycles have been presented in figure 9. For all the samples, two overlapped semicircles have been observed, which clearly reflect the multistep nature of the overall Li insertion processes. The high frequency intercept of the impedance spectrum gives ohmic resistance of the cell which includes the resistive contribution of the electrolyte (R_e), two electrodes, the current collectors and the lead wires. The low frequency intercept gives the total resistance which includes ohmic resistance of the cell, concentration polarization and mass transfer polarization resistance. The numerical value of the total diameters of the two semicircles on the Z real axis is approximately equal to the charge transfer resistance 'R_{ct}'. The straight line in the low frequency region is attributed to the diffusion (Warburg diffusion) of the ions into the bulk of the electrode material.

From figure 9, it could be observed that the charge transfer resistance decreases with increasing dopant concentration. The charge transfer resistance of the Nd-0·05 doped sample has been observed to be lower when compared to rest of the compounds. The plot of real part of impedance (Z_{re}) vs the reciprocal root square of the lower angular frequencies ($\omega^{-0.5}$) is presented in figure 10. A straight line has been obtained for all the samples. The straight line could be attributed to the diffusion (Warburg diffusion) of the lithium ions into the electrode materials and the slope of the straight line gives the Warburg coefficient (σ_w). This reason is governed by equation

$$Z_{re} = R_e + R_{ct} + \sigma_w \cdot \omega^{-0.5}, \quad (3)$$

where ω is the angular frequency in the low frequency region ($\omega = 2\pi f$).

Table 5. Electrochemical parameters.

Sample	Anodic potential (V)		Cathodic potential (V)		Discharge capacity (mAh/g)	Capacity retention (%)
	E_1	E_2	E_3	E_4		
$LiNd_{0.05}Mn_2O_4$	4·096	4·222	4·055	3·919	132·39	88·44
$LiNd_{0.10}Mn_2O_4$	4·095	4·216	4·052	3·925	126·49	97·10
$LiNd_{0.15}Mn_2O_4$	4·079	4·194	4·107	3·951	115·06	96·80

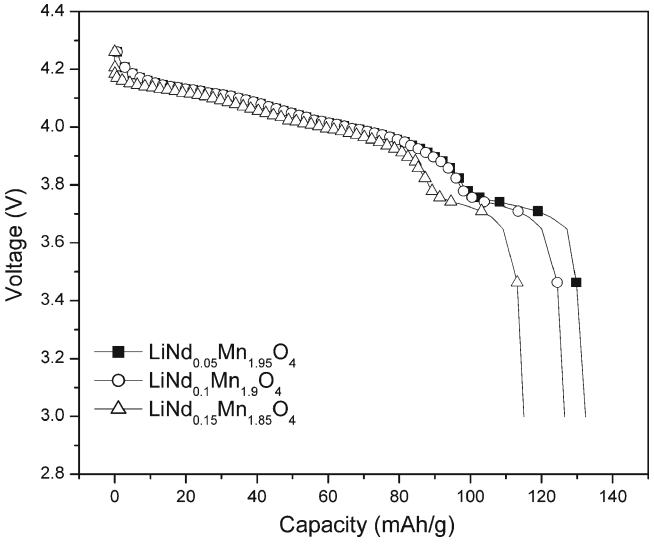

Figure 7. Discharge curve of $LiNd_xMn_{2-x}O_4$ samples.

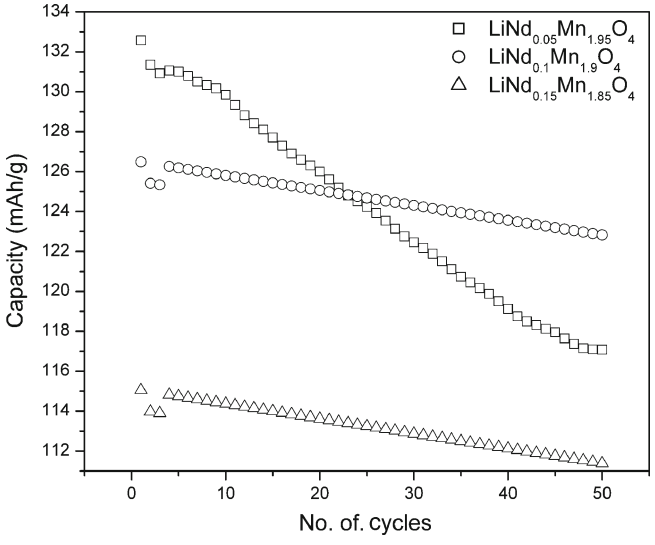

Figure 8. Cycle life of $LiNd_xMn_{2-x}O_4$ samples.

The diffusion coefficient of lithium has been calculated using Warburg coefficient and surface electrolyte interfacial capacitance (C_{dl}) as per (3)

$$D^{Li+} = 0{\cdot}5\left(RT/An2F^2\sigma_w C_{dl}\right)^2, \quad (4)$$

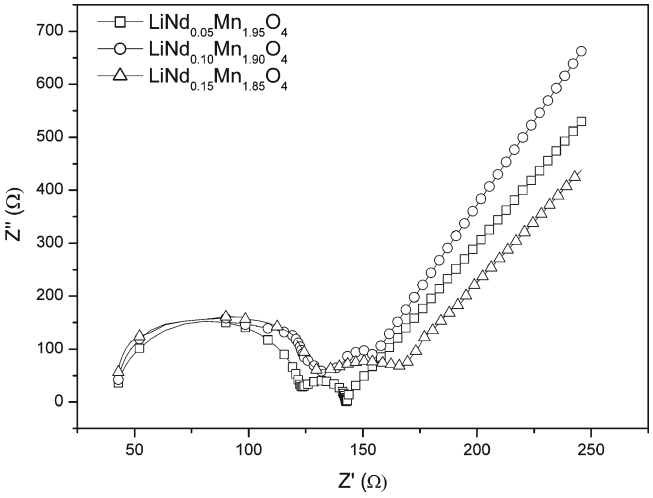

Figure 9. Nyquist plot of $LiNd_xMn_{2-x}O_4$ samples.

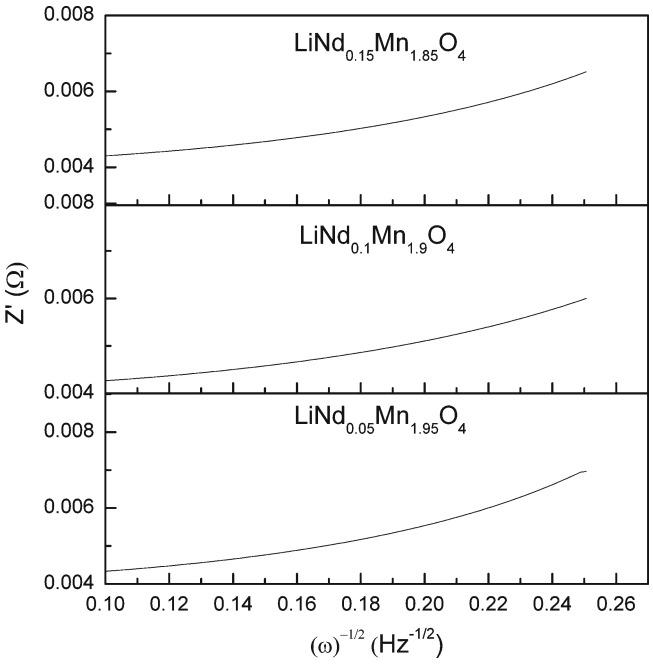

Figure 10. Warburg diffusion plot of $LiNd_xMn_{2-x}O_4$ samples.

where R is the gas constant, T the absolute temperature, F the Faraday's constant, A the area of the electrode surface and C the molar concentration of Li^+ ions. Furthermore, the exchange current density (i_0) of the reaction is given by

$$i_0 = RT/nFR_{ct}. \quad (5)$$

The values calculated using the above equations have been presented in table 6. The straight line obtained for all the samples clearly shows uniform diffusion of Li in all the compounds. From table 6, it could be observed that other than Nd-0·10 sample, the diffusion coefficient is higher for rest of the samples and the double layer capacitance reduces with increasing dopant concentration. This illustrates efficiency of the Nd^{3+} doping in arresting the resistance due to surface film formation and enhanced compatibility with the electrolyte without any structural degradation (Xia and Yoshio 1996).

4. Conclusions

XRD pattern and FT–IR spectra reveals the spinel cubic structure for all the synthesized compounds. The octahedral site preference of the Nd^{3+} dopant ion revealed by FT–IR spectra corroborates its substitution instead of Mn^{3+} ion and thus the effect due to Jahn Teller distortion is minimized. The unit cell dimension has been observed to contract with Nd^{3+} doping due to the higher binding energy between Nd–O bonds and increase in Mn^{4+} content. The particle size of all the compounds have been observed to be within 100 nm, hence the adopted synthesis condition has been observed to be well suited to prepare nanomaterials with good control over the stoichiometry. Even though the morphological analyses have revealed excessive agglomeration for Nd 0·1 sample, the increasing trend of pore aspect ratio with doping concentration would yield better electrochemical activity. The discharge profiles of the compounds have exhibited reduction in initial cycle capacity from 132 mAh/g to 115 mAh/g for the Nd^{3+} doping from 0·05 to 0·15 level, but the substitution of Nd^{3+} has positive effect on the cycle life of the electrodes. The capacity retentions after 50 cycles have been observed to be higher for both Nd 0·1 and Nd 0·15 samples. The effective reduction in double layer capacitance is observed due to doping of neodymium ions and moreover the Li ion diffusion coefficient has been observed to be higher for Nd 0·1 level doping when compared to lower level Nd^{3+} doping. Thus, this study clearly emancipates the facile nature

Table 6. Parameters from impedance spectroscopy of $LiNd_xMn_{2-x}O_4$.

Sample	Warburg coefficient (σ_w) (±0·001)	Li^+ diffusion coefficient ($\times10^{-12}cm^2s^{-1}$) (±0·1)	Double layer capacitance (μF) (±0·1)	Exchange current density (A/cm^2) (±0·01)
$LiNd_{0·05}Mn_{1·95}O_4$	0·011	0·3	9	0·19
$LiNd_{0·10}Mn_{1·90}O_4$	0·019	0·2	8	0·22
$LiNd_{0·15}Mn_{1·85}O_4$	0·013	0·3	8	0·18

of Nd^{3+} doping in increasing the shelf life of the existing commercial $LiMn_2O_4$-based Li ion batteries.

Acknowledgements

The authors express their gratitude to the Principal and Management of Thiagarajar College of Engineering, Madurai, for their support and they also thank Research Centre Imarat, Hyderabad, for financial support.

References

Arora P, Popov B N and White R E 1998 *J. Electrochem. Soc.* **145** 807

Aurbach D, Markovsky B, Levi M D, Levi E, Shechter A, Moshkovich M and Cohen C 1999 *J. Power Sources* **81–82** 95

Balaji S, Mutharasu D, Shanmugan S, Sankara Subramanian N and Ramanathan K 2010 *Ionics* **16** 351

Balasubramanian M, Lee H S, Sun X, Yang X Q, Moodenbaugh A R, Mcbreen J, Fischer D A and Fu Z 2002 *Electrochem. Solid State Lett.* **5** A22

Chung K Y and Kim K B 2004 *Electrochim. Acta* **49** 3327

Denga Bohua, Nakamura Hiroyoshi, Zhang Qing, Yoshio Masaki and Xia Yongyao 2004 *Electrochim. Acta* **49** 1823

Feng Chuanqi, Tang Hao, Zhang Keli and Sun Jutang 2003 *Mater. Chem. Phys.* **80** 573

Fey George Ting-Kuo, Lu Cheng-Zhang and Prem Kumar T 2003 *J. Power Sources* **115** 332

Image J 2002 Image processing and analysis in Java, Research Services Branch NIMH & NINDS, Available Via http://rsb.info.nih.gov/ij. Accessed 20 March 2009

Iqbal Muhammad Javed and Ahmad Zahoor 2008 *J. Power Sources* **179** 763

Julien C M and Massot M 2003 *Mater. Sci. Eng.* **B97** 217

Kerr J A 2000 *CRC handbook of chemistry and physics* (ed.) D R Lide (Boca Raton, Florida, USA: CRC Press) 81st ed. pp 9–55

Lalitha S, Sathyamoorthy R, Senthilarasu S, Subbarayan A and Natarajan K 2004 *Sol. Energ. Mater. Sol. C* **82** 187

Ma Shuhua, Noguchi Hideyuki and Yoshio Masaki 2004 *J. Power Sources* **126** 144

Modi K B 2004 *J. Mater. Sci.* **39** 2887

Molenda M, Dziembaj R, Podstawka E and Proniewicz L M 2005 *J. Phys. Chem. Solids* **66** 1761

Ohzuku T, Ariyoshi K, Takeda S and Sakai Y 2001 *Electrochem. Acta* **46** 2327

Ozawa T 1970 *J. Thermal Anal.* **2** 301

Ravinder D and Manga T 1999 *Mater. Lett.* **41** 254

Santander N, Das S R, Majumder S B and Katiyar R S 2004 *Surf. Coat. Technol.* **177–178** 60

Singhal Rahul, Das Suprem R, Tomar Maharaj S, Ovideo Osbert, Nieto Santander, Melgarejo Ricardo E and Katiyar Ram S 2007 *J. Power Sources* **164** 857

Thackeray M M, David W I F, Bruce P G and Goodenough J B 1983 *Mater. Res. Bull.* **18** 461

Thackerey M M and Rossouw M H 1994 *J. Solid State Chem.* **113** 441

Thamizhmani G, Dodelet J P and Guay D 2004 *J. Electrochem. Soc.* **143** 18

Waldron R D 1955 *Phys. Rev.* **99** 1727

Xia Y and Yoshio M 1996 *J. Electrochem. Soc.* **143** 825

Xia Y, Zhou Y and Yoshio M 1997 *J. Electrochem. Soc.* **144** 2593

Yang S T, Jia J H, Ding L and Zhang M C 2003 *Electrochim. Acta* **48** 569